AIAA JOURNAL
Vol. 46, No. 9, September 2008

Detached-Eddy Simulation Around a Forebody with Rotary Motion

Aroon K. Viswanathan and Kyle D. Squires
Arizona State University, Tempe, Arizona 85287-6106
and
James R. Forsythe
Cobalt Solutions, LLC, Springfield, Ohio 45504

DOI: 10.2514/1.4756

Predictions of the massively separated flow around a rectangular ogive forebody are obtained using detached-eddy simulation and from a solution of the unsteady Reynolds-averaged Navier–Stokes equations. The lengths of the forebody and aftbody are 2 and 4 times the body diameter, respectively. Angles of attack of 60 and 90 deg are considered, the Reynolds number based on freestream speed and diameter is 2.1×10^6, and the freestream Mach number is 0.21. Computations of the static geometry and of the ogive undergoing prescribed rotary motion are performed on a range of meshes with grid refinement from 2.1×10^6 to 8.75×10^6 cells. Flow visualizations of the instantaneous vorticity show that the detached-eddy simulation predictions exhibit an increase in the range of resolved scales with increased mesh resolution. Detached-eddy simulation predictions of the pressure distribution at axial stations along the forebody are in good agreement with measured values for both angles of attack. Unsteady Reynolds-averaged Navier–Stokes predictions of the pressure along the forebody for 90 deg angle of attack exhibit relatively strong coherence, with the resulting pressure variation different from the measured values and detached-eddy simulation results. Detached-eddy simulation predictions of the ogive experiencing rotary motion about its center are obtained for spin coefficients of 0.1 and 0.2 at 90 deg angle of attack. Agreement between the predicted and measured pressure distributions for these cases is less satisfactory compared to the static-geometry results.

Nomenclature

C_p = pressure coefficient
D = main body diameter
d = distance to the nearest solid wall
$\tilde{d}$ = turbulence length scale
L = total length of the forebody, main body, and aftbody
Re = Reynolds number based on freestream velocity and body diameter D
U_∞ = freestream velocity
x = coordinate aligned with the long axis of the ogive
y = coordinate aligned with the freestream velocity
y = coordinate perpendicular to the long axis of the ogive
α = angle of attack
Δ = largest distance between neighboring cell centers
θ = angle around the forebody
ν = kinematic fluid viscosity
ν_t = kinematic eddy viscosity
Ω = rotation rate

I. Introduction

MANY flows of technological interest occur at high Reynolds number and are often characterized by regions of massive separation. Examples relevant to the present contribution include the forebody of fighter aircraft at high angles of attack for which flow separation and Reynolds number effects are important, for example, as relates to stability, control, and maneuverability. Simulation and modeling applied to these flows is a useful tool to advance understanding of particular phenomena and eventually as an integral component for routine analysis and design. Unfortunately, prediction of massively separated flows at high Reynolds numbers continues to challenge most simulation strategies and, in general, the performance of computational fluid dynamics (CFD) in predicting massively separated flows has been less than reliable.

Most predictions of high-Reynolds number turbulent flows are obtained from solutions of the Reynolds-averaged Navier–Stokes (RANS) equations. Although the most popular RANS models appear to yield predictions of useful accuracy in attached flows as well as some with shallow separations, RANS predictions of massively separated flows have typically been unreliable. RANS models, calibrated in thin shear layers, appear unable to consistently represent to sufficient accuracy the geometry-dependent, chaotic, and unsteady features of massive separations. The relatively poor performance of RANS models motivates the application of techniques such as large eddy simulation (LES). Away from solid surfaces, LES is a powerful approach, providing a description of the large, energy-containing scales of motion that are typically dependent on geometry and boundary conditions. When applied to boundary layers, however, the computational cost of whole-domain LES does not differ significantly from that of direct numerical simulation (DNS) [1].

The need for computationally feasible and accurate simulation techniques for massively separated flows at high Reynolds numbers has provided much of the impetus for the development of hybrid RANS-LES strategies. Such methods attempt to capitalize on the most favorable aspects of each method by restricting RANS to the prediction of attached boundary layers and LES to the treatment of separated regions [1]. One of the more popular hybrid RANS-LES methods, and the main focus of the present effort, is detached-eddy simulation (DES) [2]. The DES formulation used in this work is based on a modification to the Spalart–Allmaras one-equation model [3] (referred to as SA throughout) and described in greater detail in the following section. In natural DES applications, the entire boundary layer is predicted using a RANS model; a change to the length scale in the wall-destruction term of the SA model leads to a Smagorinsky-like subgrid-scale viscosity away from solid surfaces.

Presented as Paper 0265 at the Aerospace Sciences Meeting, Reno, Nevada, 6–9 January 2003; received 22 August 2003; revision received 30 October 2005; accepted for publication 29 December 2005.

Nearly all hybrid RANS-LES methods, including the original version of DES developed by Spalart et al. [2], achieve an LES character by introducing the grid spacing into the turbulence model (e.g., see also the limited numerical scales formulation of Batten et al. [4]). The recent study of the supersonic base flow reported by Kawai and Fuji [5] provides a representative example of a comprehensive investigation using a hybrid RANS-LES approach. In [5] the RANS and LES models were based on eddy viscosity formulations and with a function introduced to control the blending width of the RANS and LES regions.

DES predictions are obtained in this work using Spalart–Allmaras as the base model, identical to the original formulation proposed by Spalart et al. [2]. In DES, the interface between the "RANS region" and "LES region" is dependent on the local mesh spacing and distance from the wall. Previous applications of the technique have been favorable, yielding adequate predictions across a range of flows and also showing the computational cost has a weak dependence on Reynolds number, similar to RANS methods yet at the same time providing more realistic descriptions of unsteady effects (e.g., see Travin et al. [6], Forsythe et al. [7], Constantinescu and Squires [8]).

The specific flow considered is that around a rectangular ogive forebody, cross sections are shown in Fig. 1. The length of the aft section is 4 times the width ("diameter," D), the cross section being a rounded square in which the corner radius is $1/4$ of the width (similar to the cross sections of the X-29 and T-38) and with a hemispherical end cap. The length of the forebody (ogive cone) is twice the diameter, with a similar cross section as the main body. The rotary balance measurements of Pauley et al. [9] are used to assess the simulation results. From the experiments, an extensive database on circular and ogive forebodies was compiled using measurements acquired in a pressurized wind tunnel that enabled a variation in the Reynolds number from 8×10^4 to 2.25×10^6 (based on the freestream speed and diameter D). Angles of attack $\alpha = 60$ deg and 90 deg were considered in addition to cases with prescribed rotary motion for which the spin coefficient $\Omega L/(2U_\infty)$ was varied between ± 0.4 for some of the cases. Pauley et al. [9] reported force and moment measurements along with pressure distributions at axial stations along the bodies. Van Dam et al. [10] reported computations of the flow around both the circular and rectangular ogive at 60 deg angle of attack and for a spin coefficient of -0.2. Most of the solutions in that effort were from the steady RANS equations using the Baldwin–Lomax model with additional calculations performed using SA. In general, reasonable agreement between measured and predicted pressure distributions was reported.

Both static-geometry and rotary-motion cases are reported in the present contribution. Pauley et al. [9] found that flow attachment along the forebody was correlated to the local Reynolds number, which varied with width, measurements showing that $Re > 2 \times 10^5$ was required for attached flow on the forebody. Flowfield characteristics also exhibited a relatively strong dependence on Reynolds number up to around 5×10^5. In the present investigation, the computations are performed at $Re = 2.1 \times 10^6$ (based on freestream velocity and the body diameter).

The next section summarizes the turbulence model and numerical procedures. Following in the Results section is first a description of the predictions of the flow around the static geometry at 60 deg angle of attack, followed by the simulation results for the static-geometry and rotary-motion cases for angle of attack $\alpha = 90$ deg. A summary and perspectives developed from the work are then presented.

II. Approach

A. Detached-Eddy Simulation

The DES formulation employed in this work is based on a modification to the Spalart–Allmaras RANS model [3] such that the model reduces to its RANS formulation near solid surfaces and to a subgrid model away from the wall [2]. The SA RANS model solves an equation for the variable $\tilde{\nu}$ which is dependent on the turbulent viscosity. The model is derived based on empiricism and arguments of Galilean invariance, dimensional analysis, and dependence on molecular viscosity. The model includes a wall-destruction term that reduces the turbulent viscosity in the wall layer and trip terms to provide smooth transition to turbulence. The transport equation for the working variable $\tilde{\nu}$ used to form the eddy viscosity takes the form,

$$\frac{D\tilde{\nu}}{Dt} = c_{b1}\tilde{S}\,\tilde{\nu} - c_{w1}f_w\left[\frac{\tilde{\nu}}{d}\right]^2 + \frac{1}{\sigma}\{\nabla\cdot[(\nu+\tilde{\nu})\nabla\tilde{\nu}] + c_{b2}(\nabla\tilde{\nu})^2\} \quad (1)$$

where $\tilde{\nu}$ is the working variable. Equation (1) is written without the terms that can be employed to trip (i.e., activate) the model at desired locations along a body. As also discussed in Sec. II.B, the present effort focuses on the highest Reynolds number for which experimental measurements are available. This choice should lessen the dependence of the solutions on influences of transition from laminar-to-turbulent flow. In particular, the present computations presume that the boundary layers on the forebody are fully turbulent, an approximation that becomes increasingly accurate at higher Reynolds numbers. Note that if the transition locations were available from the experimental measurements, then it would be possible to activate the SA model at the corresponding positions using the trip terms.

The eddy viscosity ν_t is obtained from

$$\nu_t = \tilde{\nu} f_{v1}, \qquad f_{v1} = \frac{\chi^3}{\chi^3 + c_{v1}^3}, \qquad \chi \equiv \frac{\tilde{\nu}}{\nu} \quad (2)$$

where ν is the molecular viscosity. The production term is expressed as

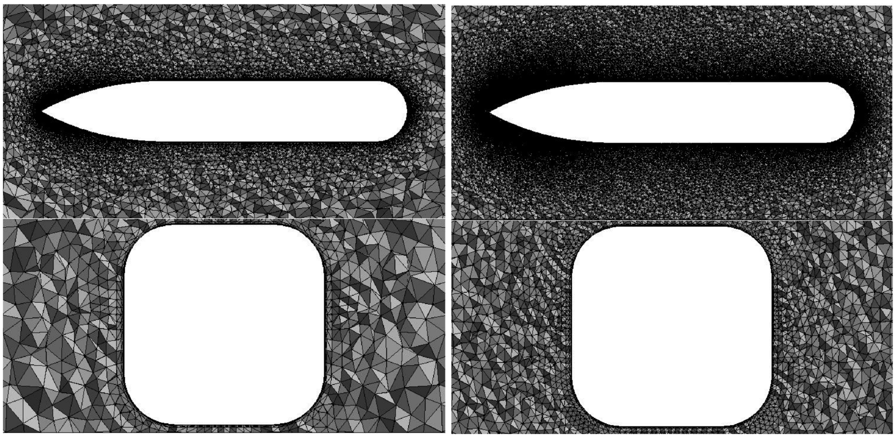

a) b)

Fig. 1 Side and end views of the a) coarse grid (2.1×10^6 cells) and b) fine grid (8.75×10^6 cells). Length of the forebody is twice the width/diameter (D), and the length of the aft body is $4D$. The cross section is a rounded square with corner radius $= D/4$.

$$\tilde{S} \equiv S + \frac{\tilde{\nu}}{\kappa^2 d^2} f_{v2}, \qquad f_{v2} = 1 - \frac{\chi}{1 + \chi f_{v1}} \tag{3}$$

where S is the magnitude of the vorticity. The function f_w is given by

$$f_w = g\left[\frac{1 + c_{w3}^6}{g^6 + c_{w3}^6}\right]^{1/6}, \qquad g = r + c_{w2}(r^6 - r), \qquad r \equiv \frac{\tilde{\nu}}{\tilde{S}\kappa^2 d^2} \tag{4}$$

The wall boundary condition is $\tilde{\nu} = 0$. The constants are $c_{b1} = 0.1355$, $\sigma = 2/3$, $c_{b2} = 0.622$, $\kappa = 0.41$, $c_{w1} = c_{b1}/\kappa^2 + (1 + c_{b2})/\sigma$, $c_{w2} = 0.3$, $c_{w3} = 2$, $c_{v1} = 7.1$, and $c_{v2} = 5$.

The DES formulation is obtained by replacing in the SA model the distance to the nearest wall d, by $\tilde{d}$, where $\tilde{d}$ is defined as

$$\tilde{d} \equiv \min(d, C_{\mathrm{DES}}\Delta) \tag{5}$$

In Eq. (5), Δ is the largest distance between the cell center under consideration and the cell center of the neighbors (i.e., those cells sharing a face with the cell in question). In natural applications of the technique, the wall-parallel grid spacings (e.g., streamwise and spanwise) are comparable to the boundary layer thickness and the SA RANS model is retained through most, or all, of the boundary layer, that is, $\tilde{d} = d$. Consequently, the prediction of boundary layer separation is determined in the "RANS mode" of DES. Away from solid boundaries, the closure is a one-equation model for the subgrid-scale eddy viscosity. When the production and destruction terms of the model are balanced, the length scale $\tilde{d} = C_{\mathrm{DES}}\Delta$ in the LES region yields a Smagorinsky-like eddy viscosity $\tilde{\nu} \propto S\Delta^2$. The additional model constant $C_{\mathrm{DES}} = 0.65$ was set in homogeneous turbulence [11] and used without modification in this work.

B. Simulation Overview

The compressible Navier–Stokes equations are solved on unstructured grids using *Cobalt* [12]. The numerical method is a cell-centered finite volume approach applicable to arbitrary cell topologies (e.g., hexahedron, prisms, tetrahedron). The spatial operator uses the exact Riemann solver of Gottlieb and Groth [13], least squares gradient calculations using QR factorization to provide second-order accuracy in space, and total variation diminishing (TVD) flux limiters to limit extremes at cell faces. A point implicit method using analytical first-order inviscid and viscous Jacobians is used for advancement of the discretized system. For time-accurate computations, a Newton subiteration scheme is employed, and the method is second order accurate in time. The domain decomposition library ParMETIS [14] is used for parallel implementation and communication between processors is achieved using a message passing interface.

Simulation of rigid-body motion is achieved using an arbitrary Lagrangian Eulerian (ALE) formulation, where the grid is neither stationary nor follows the fluid motion [15]. The conservation equations are solved in an inertial reference frame with the spatial operator modified in order that the advection terms are relative to the (noninertial) grid reference frame. This requires simple modifications to many boundary conditions and to the initial conditions for the Riemann problem. At the beginning of a time step, all geometric quantities are transformed to their values at the end of the given time step, according to the specified motion. This ensures the fluxes, which an implicit scheme computes at the end of the time step, are consistent with the geometry. The number of Newton subiterations was increased compared to the static-geometry cases (from three to five, based on findings from preliminary computations) in order to reduce errors associated with integrating over the time step with an implicit temporal operator.

Computations were carried out on a cubic domain that extends from the origin, located at the centroid of the ogive, to around 10 times the ogive length (thus, approximately 60 forebody diameters). Far-field conditions on the flow variables were prescribed at the outer boundaries of the computational domain using Riemann invariants. The coordinate system origin is fixed to the nose of the forebody with x aligned with the long axis of the ogive, y aligned with the freestream velocity when $\alpha = 90$ deg, and z completing the right-hand rule. Solutions of the fully turbulent flow at $Re = 2.1 \times 10^6$ are presented in the following sections for angles of attack of 60 and 90 deg. The fully turbulent solution is obtained by prescribing at the inlet to the computational domain a small level of eddy viscosity (corresponding to $\chi = 3$), sufficient to ignite the turbulence model as the fluid enters the boundary layers.

The computations were performed on unstructured grids generated using VGRIDns [16]. The grid was clustered near the ogive surface and geometrically stretched at a rate of 1.2 away from the wall, the distance from the wall to the first cell center was less than $2 \times 10^{-6} D$, within one viscous unit on average. Grid refinement was accomplished via variation of the parameter *ifact* in VGRIDns, enabling an efficient and uniform refinement in all directions. Computations were performed on a series of four grids, a baseline mesh composed of approximately 6.5×10^6 cells, a fine grid with around 8.75×10^6 cells, and two coarser meshes composed of approximately 2.1×10^6 cells (coarse) and 3.5×10^6 cells. Cross sections showing the coarse and fine grids are shown in Fig. 1. Defining a flow time scale using the ogive diameter D and freestream velocity, DES predictions on the baseline grid were sampled for over 100 time units, the dimensionless time step was 0.025.

III. Results

A. 60 Deg Angle of Attack—Static Geometry

Shown in Fig. 2 are contours of the instantaneous eddy viscosity ratio (ratio of the turbulent eddy viscosity to the molecular viscosity) in axial planes along the forebody. The prediction shown in Fig. 2 is obtained using DES on the baseline mesh of 6.5×10^6 cells and indicates that the flow remains attached around the "vertical" faces of the ogive (sides that are parallel to the freestream velocity), with separation apparent in the leeward region. The contours in Fig. 2 show that the wake is coherent and characterized by a pair of counter-rotating structures. The surface pressure shown on the body further illustrates the relatively strong influence of the structures on the pressure distribution, the striations correlated to the presence of the vortical structure over the forebody.

A comparison of the pressure distributions in six axial planes along the forebody predicted using DES and SA URANS to the experimental measurements are shown in Figs. 3–5. Defining x from the nose of the forebody, the predictions are compared to the measurements at $x/L = 0.027$, 0.055, 0.111, 0.166, 0.222, and 0.305 (corresponding to the six axial planes on the forebody shown in Fig. 2). In Figs. 3–5 and throughout the manuscript the pressure coefficient is defined using the freestream density, pressure, and

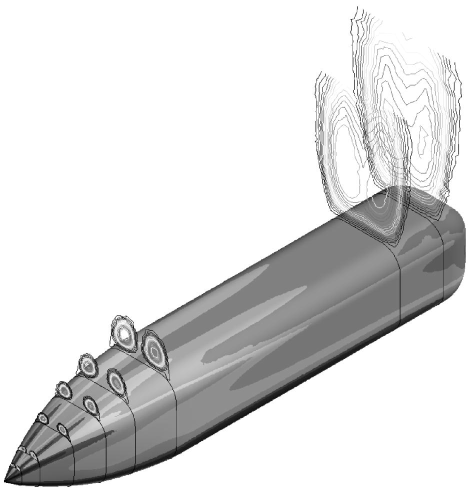

Fig. 2 Ratio of the instantaneous eddy viscosity to the molecular value at the eight axial locations for which pressure distributions are measured. DES prediction on the baseline grid, $\alpha = 60$ deg, surface colored by pressure.

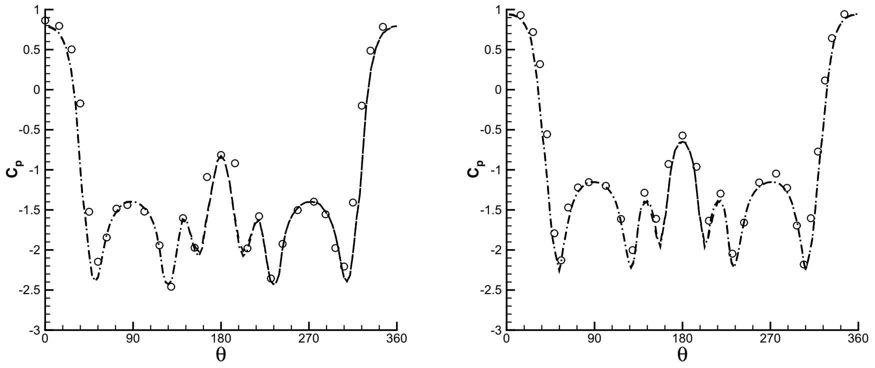

a) b)

Fig. 3 Pressure coefficient for $\alpha = 60$ deg at a) $x/L = 0.027$ and b) $x/L = 0.055$. ○: measurements; dash-dotted line: DES; dashed line: URANS.

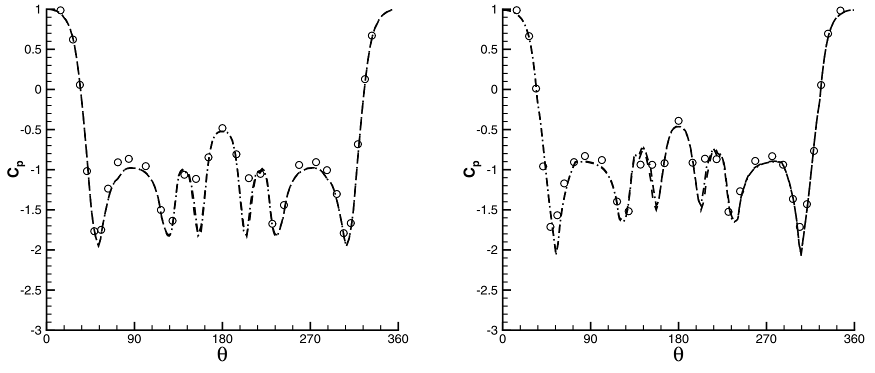

a) b)

Fig. 4 Pressure coefficient for $\alpha = 60$ deg at a) $x/L = 0.111$ and b) $x/L = 0.166$. ○: measurements; dash-dotted line: DES; dashed line: URANS.

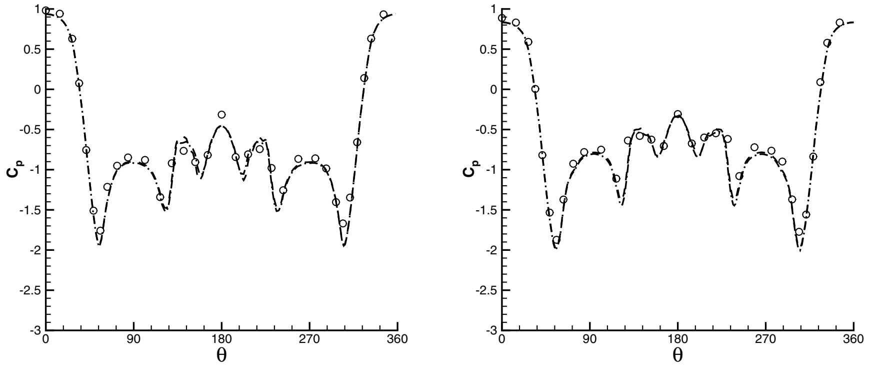

a) b)

Fig. 5 Pressure coefficient for $\alpha = 60$ deg at a) $x/L = 0.222$ and b) $x/L = 0.305$. ○: measurements; dash-dotted line: DES; dashed line: URANS.

velocity. The angle θ around the forebody is measured positive in the clockwise direction with $\theta = 0$ corresponding to the windward symmetry plane. In general, the measured pressure distribution shown in the figures is consistent with the visualization in Fig. 2 indicating attached flow to the rear surface and coherent structures in the separated region. The measured pressures in Figs. 3–5 exhibit minima in the corner regions, that is, in the vicinity of $\theta \approx 45$, 135, 225, and 315 deg as well as on the leeward face due to the influence of the separated structures in the wake ($135 < \theta < 225$ deg). In addition, at each axial location the second pressure maxima occurs in the aft region in the leeward symmetry plane, $\theta = 180$ deg.

The predictions exhibit reasonable or good agreement with the measurements reported by Pauley et al. [9]. At the third and fourth axial station from the nose (c.f., Fig. 2), the simulation results in Fig. 4 show that there is a strong angular dependence of the pressure in the vicinity of $\theta \approx 180$ deg. The variation in the pressure coefficient in that region is stronger in the predictions than indicated by the measurements, though possibly consistent with insufficient resolution in the pressure measurements. Also apparent from the figures is that the DES and URANS predictions of the averaged pressure distributions are essentially the same, the results obtained for $\alpha = 60$ deg using the baseline grid. Differences between the two simulation techniques are illustrated in the temporal evolution of the axial (aligned with the long axis of the ogive) and normal (orthogonal to the long axis of the ogive) forces shown in Fig. 6. The figure shows that the DES predictions of the forces fluctuate in time due to vortex shedding as compared to the virtually steady URANS results. Given the good agreement between the DES and URANS pressure distributions on the forebody (c.f., Fig. 5) the differences in the force histories in Fig. 6 might seem surprising. However, the force histories represent the integrated effect of the pressure and shear stresses over the entire body and the (time-averaged) pressure

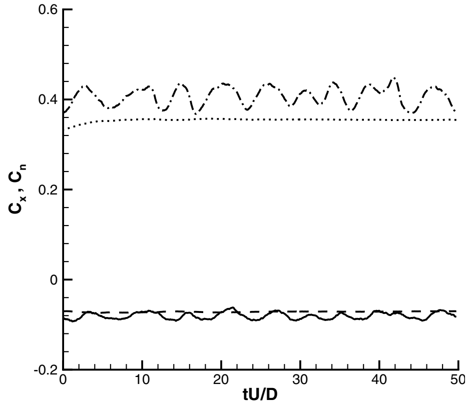

Fig. 6 DES and URANS predictions of the axial (aligned with the long axis of the ogive) and normal (orthogonal to the long axis of the ogive) forces, baseline grid, $\alpha = 60$ deg. DES: solid line, axial; dash-dotted line, normal. URANS: dashed line, axial; dotted line, normal.

distributions are only over the forebody section. For both the time-averaged axial and normal forces, the difference between the DES and URANS predictions is less than 15%. Figure 6 shows the influence of vortex shedding most clearly in the normal force histories with the dominant frequency corresponding to a shedding Strouhal number around 0.25.

B. 90 Deg Angle of Attack—Static Geometry

Shown in Fig. 7 are contours of the eddy viscosity ratio along the ogive for $\alpha = 90$ deg. The ogive surface is colored by the instantaneous pressure in Fig. 7. On the leeward side of the ogive, the URANS prediction shows that the wake is composed of a pair of coherent counter-rotating vortical motions, as evidenced by the contours of the eddy viscosity in the planes and the signature of these structures on the surface pressure, especially along the forebody. The DES prediction, on the other hand, exhibits a more chaotic structure in the planes along the forebody. Also apparent is the more uniform pressure on the leeward surface of the forebody, the figure showing a marked difference compared to the URANS result. Given that the agreement between the measured and predicted pressures is much more favorable for the DES than the URANS as shown later, one can infer that the wake structure highlighted by Fig. 7 is more accurately captured in the DES.

The structure of the wake and influence of the grid is illustrated in Fig. 8 where contours of the instantaneous vorticity magnitude are plotted in the plane $x/L = 0.5$ for the coarse, baseline, and fine grids as well as the URANS result (obtained using the baseline grid). In general, and analogous to the behavior observed in other DES predictions of bluff-body flows [6], increases in mesh density lead to a wider range of scales resolved in the wake. The fine-grid result exhibits a wider range of eddy content than captured in the coarse-grid DES prediction, with the prediction obtained on the baseline mesh exhibiting a range of scales intermediate to those obtained on the coarse and fine grids. The URANS result in the lowest frame shows relatively short shear layers that are diffused in the near wake; the structure of the coarse-grid DES prediction (Fig. 8a) is somewhat similar to that of the URANS.

The vorticity in a plane normal to the freestream velocity and downstream of the ogive is shown in Fig. 9. The DES predictions, and to a lesser extent the URANS result, show a tapering of the wake toward the forebody. Figure 9 also shows that, moving from the top to the third frame, the influence of grid refinement increases the scale range resolved in the wake, as also shown in Fig. 8. For the plane shown, the DES solutions exhibit substantial variation along the axial ("spanwise") coordinate, and the figure also shows that axial variation is apparent in the URANS result.

In DES, the RANS and LES regions are delineated based on the local grid length scale compared to the wall distance. Figure 10 shows the variation of the turbulent length scale $\tilde{d}$ and the eddy viscosity ratio plotted against wall distance d in the plane $x/L = 0.5$. The profiles shown in the figure are from the leeward corner slightly upstream of flow separation and from calculations performed on the baseline grid. The increase in the length scale $\tilde{d}$ initially follows the wall distance until the local grid length scale becomes sufficiently small compared to d to determine $\tilde{d}$ [cf., Eq. (5)]. Outside the RANS-LES interface (defined as the location at which $\tilde{d}$ is set by Δ) the turbulent length scale continues to slightly increase before eventually becoming essentially constant. Figure 10 also shows that the RANS and DES eddy viscosities are very similar from the wall to the interface. Outside the interface, the DES eddy viscosity initially decreases more slowly than the RANS value, eventually decreasing with increasing distance from the wall due to the more pronounced effect of the destruction term in the model.

Shown in Fig. 11 are DES and URANS predictions of the time histories of the forces and yawing moment for simulations performed using the baseline grid (the coefficients are defined using the area DL). Note that in Fig. 11 only a portion of the temporal evolution (25 time units) is shown for clarity, and averages were acquired over 100 time units. In general, the temporal variation in the forces and yawing moment from the URANS is substantially lower than achieved in the DES. As shown in Fig. 11a, the streamwise (drag) force from the URANS, while for the most part consistently higher, does not differ drastically from the DES prediction with the averaged drag coefficient from the URANS equal to 0.334 and that for the DES on the baseline grid of 0.321. The three dimensionality developed in the URANS, although not as pronounced as in the DES (cf., Fig. 7), seems sufficient such that the structural features affecting the drag can be taken roughly into account (e.g., see Shur et al. [17]). The variations in the mean drag and mean axial force along with the rms values of the side force and yawing moment are summarized in Tables 1 and 2. As shown in Table 1, the range in

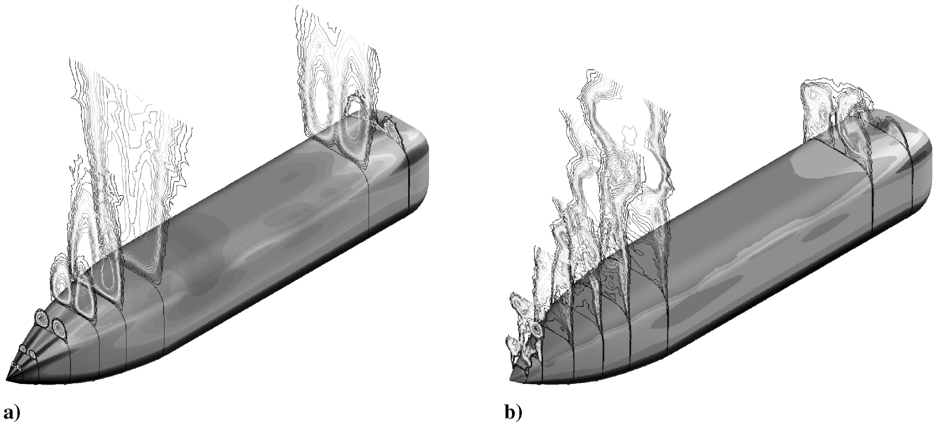
a)
b)

Fig. 7 Ratio of the instantaneous eddy viscosity to the molecular value at the eight axial locations for which pressure distributions are measured. Angle of attack of the freestream $\alpha = 90$ deg. a) URANS; b) DES. Surface colored by pressure.

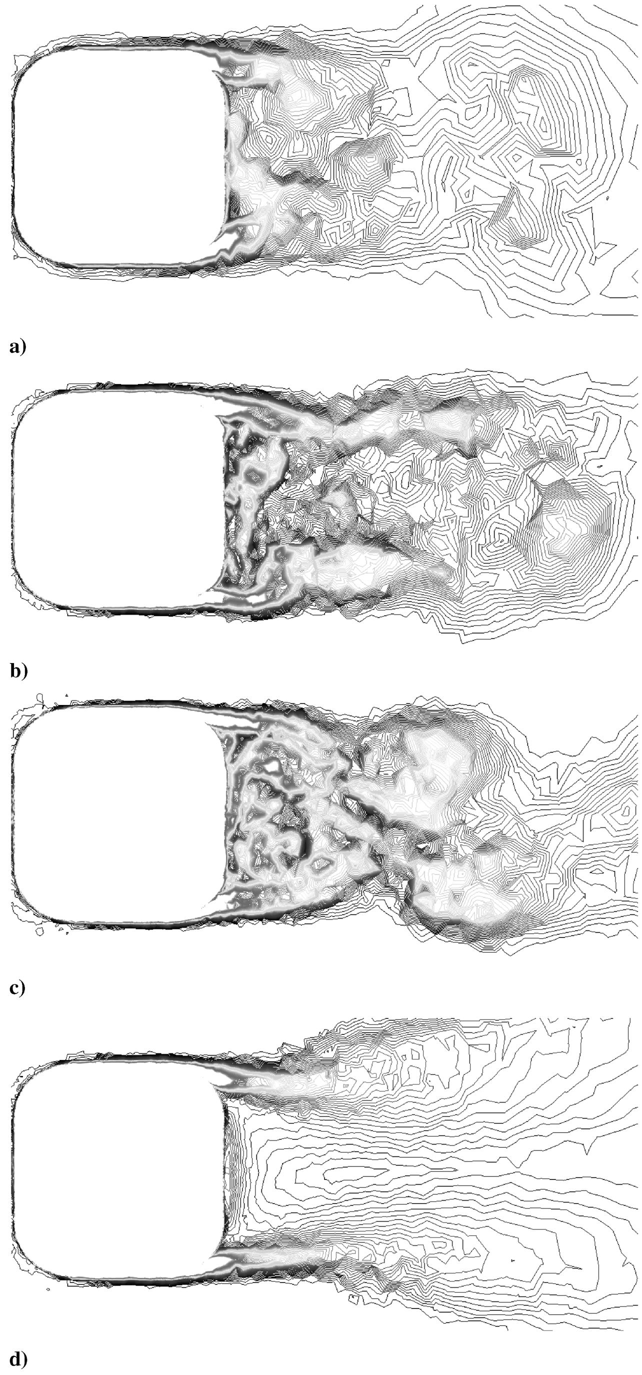

Fig. 8 Contours of the instantaneous vorticity magnitude at $x/L = 0.5$. a) Coarse grid; b) baseline grid; c) fine grid; d) URANS (baseline grid).

the averaged drag for the DES predictions over the grid resolutions considered is not large, varying by less than 1% from the coarse to the fine grid.

The development of the axial force and yawing moment in Fig. 11b in the DES and URANS exhibit similar features, with markedly larger variation with time in the DES predictions compared to the URANS result. The largest differences in forces occur in the prediction of the axial value (aligned with the long axis of the ogive). As shown in Fig. 11b, the axial force from the DES is larger, nearly a factor of 4 in the mean, as compared to the URANS result (see also Table 1). The difference arises because of the changes in flow structure illustrated previously. Figure 7, for example, shows that the DES prediction of the pressure distribution over the leeward side of the ogive is more uniform compared to the URANS. As shown later, the overall pressure along the forebody section is higher than achieved in the URANS, leading to a larger axial force.

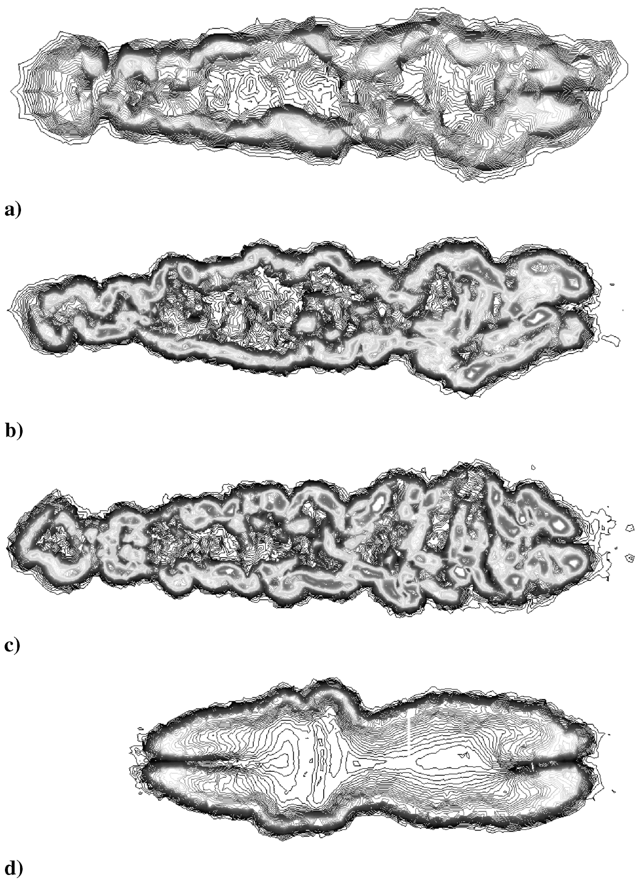

Fig. 9 Contours of the instantaneous vorticity magnitude in the plane $y = D$, view is normal to the freestream velocity. a) Coarse grid; b) baseline grid; c) fine grid; d) URANS (baseline grid).

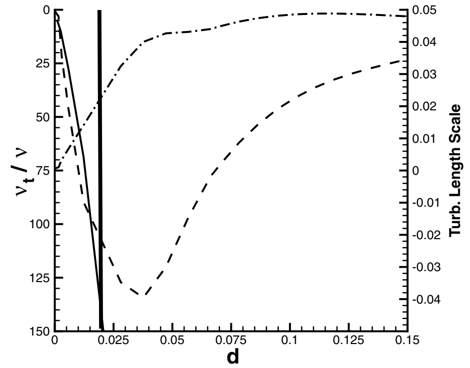

Fig. 10 Profile of the eddy viscosity ratio from the DES and URANS and the turbulent length scale $\tilde{d}$ for the DES prediction on the baseline grid at $x/L = 0.5$. The vertical line identifies the RANS-LES interface at $d = 0.019$ in the figure. Eddy viscosity ratio: solid line, RANS; dashed line, DES; dash-dotted line, turbulent length scale.

Comparisons of DES and URANS predictions of the pressure coefficient for $\alpha = 90$ deg at the six stations along the forebody are shown in Figs. 12–14. Minima in the pressure coefficient are measured in the vicinity $\theta = 48$–56 deg and $\theta = 303$–310 deg as the flow accelerates around the windward corners. Comparison of Figs. 12–14 shows that the magnitudes of the suction are mostly constant, with minimum C_p around -2.25 to -2.45. Another pair of suction minima in C_p are observed as the flow negotiates the corners on the leeward side at angles $\theta = 118$–120 deg and $\theta = 240$–242 deg. The figures show that these secondary minima are more pronounced moving from the nose ($x/L = 0.027$) toward the aft region ($x/L = 0.305$).

Before separation, prediction of the fully turbulent flow as established in these calculations by introducing nonzero eddy

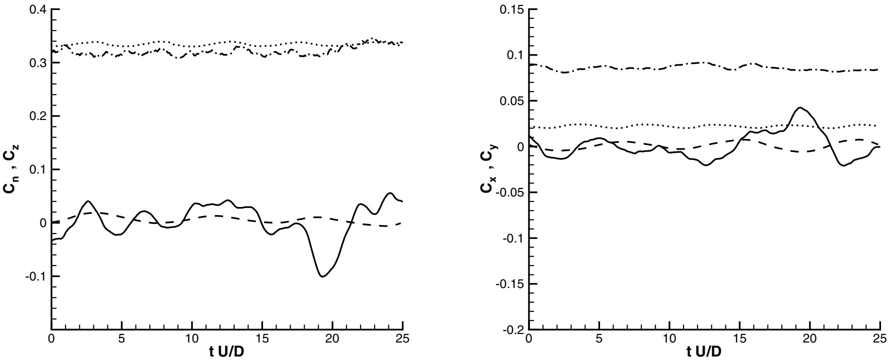

a) b)

Fig. 11 DES and URANS predictions on the baseline grid of the streamwise (drag) and side force histories a) and the yawing moment and axial force histories b), $\alpha = 90$ deg. a) Streamwise force: dash-dotted line, DES; dotted line, URANS. Side force: solid line, DES; dashed line, URANS. b) Yawing moment: solid line, DES; dashed line, URANS. Axial force: dash-dotted line, DES; dotted line, URANS.

viscosity at the inlet results in attached flow around the windward corners, as apparent in Figs. 12–14. On the forebody, separation is predicted at angles $\theta \approx 127$–132 deg and $\theta \approx 229$–232 deg, with the measured C_p uniform in the separated region on the forebody.

With the exception of the first axial station (Fig. 12a), DES predictions of the pressure distribution are in excellent agreement with the experimental measurements. The structureless, attached boundary layers predicted by the RANS model detach into the LES region that corresponds nominally to the leeward side of the forebody (i.e., the region of uniform pressure in the vicinity of $\theta \approx 180$ deg). The discrepancy between measurements and DES predictions at $x/L = 0.027$ could be a result of factors that are inherent to the physical experiment and not accounted for in the simulations as constructed. For example, any regions of laminar boundary layer in the physical experiment cannot be replicated in the current simulation setup, which established a fully turbulent solution by seeding a small level of inlet eddy viscosity. Another factor that may also contribute to the mismatch between the DES result and measurements is the influence of the grid, for example, the RANS-LES interface.

Figures 12–14 also show that the URANS predictions approach the measurements for larger x/L. For the stations nearest the nose of the forebody the URANS predictions are noticeably poor, exhibiting significant variation with θ that arises because of the coherent structures that dominate the wake and strongly influence the pressure in the leeward region (cf., Fig. 7). The very good agreement between URANS and the measurements at $x/L = 0.305$ (Fig. 14b) is probably a consequence of the three-dimensional character of the URANS, which related studies have shown is an important ingredient for accurate prediction of mean quantities (Shur et al. [17]).

Table 1 Predicted mean axial and streamwise (drag) force coefficients, static geometry, $\alpha = 90$ deg

Case	Axial force	Streamwise force
DES coarse grid	0.083	0.324
DES baseline grid	0.086	0.321
DES fine grid	0.085	0.322
URANS baseline	0.022	0.334

Table 2 Predicted rms side force and yawing moment, static geometry, $\alpha = 90$ deg

Case	rms side force	rms yawing moment
DES coarse grid	0.031	0.016
DES baseline grid	0.035	0.020
DES fine grid	0.037	0.019
URANS baseline	0.0068	0.0043

C. 90 Deg Angle of Attack—Rotary Motion

A qualitative view of the influence of rotary motion of the forebody on the structure of the wake is shown in Fig. 15. Contours of the instantaneous vorticity magnitude at three axial planes along the ogive are shown in the figure. The results are from a DES prediction obtained at a spin coefficient of 0.2 and using the baseline grid. In Fig. 15, the upper frame is on the forebody section at $x/L = 0.222$, the middle frame corresponding to $x/L = 0.5$ (the plane containing the axis about which the ogive is rotating), and the lower frame at $x/L = 0.805$. The influence of rotation on the vorticity shed into the wake is apparent, with the skewing toward opposite sides on the front and rear portions of the body as dictated by the motion.

DES predictions of the pressure distribution along the forebody for spin coefficients of 0.1 and 0.2 are compared to the experimental measurements of Pauley et al. [9] in Figs. 16–18. Analogous to the behavior observed in the vorticity contours in Fig. 15, pressure distributions show the influence of the rotary motion and are not symmetric about $\theta = 0$ deg. The minimum pressure occurs in the vicinity of the rear windward corner $\theta \approx 315$ deg in the figures (relative to the induced velocity normal to the freestream flow). The measurements also demonstrate the increasingly significant influence of rotation toward the nose of the forebody, that is, the strongest asymmetry in the pressure distribution is apparent at $x/L = 0.027$ in Fig. 16a with the measurements at $x/L = 0.0305$ in Fig. 18b exhibiting relatively greater symmetry about the plane $\theta = 0$. In addition and as expected, the asymmetry in the pressure distribution is more significant at the higher rotation rate.

The most significant disagreement between simulation and experiment is observed in Fig. 16. The DES predictions at both $x/L = 0.027$ and $x/L = 0.055$ are indicative of flow separation toward the windward side ($\theta \approx 315$ deg), rather than the attached flow indicated by the measurements. The agreement improves in Fig. 17 which shows that at $x/L = 0.111$ the minima in C_p near the windward corners are more adequately recovered compared to the measured values for both rotation rates. The relatively uniform pressure distribution for $135 < \theta < 225$ deg is also predicted in the simulations, though at $x/L = 0.111$ the figure shows the influence of flow separation in the vicinity of $\theta \approx 225$ deg in the DES and not indicated by the measurements.

At $x/L = 0.166$, shown in Fig. 17b, there is good agreement between DES predictions and the measured pressure distribution, the minima in C_p around both windward corners is recovered, and the prediction for the region with the most negative C_p is improved compared to that at $x/L = 0.111$. The magnitude of the suction at the rear windward corners increases for the higher rotation case and the suction C_p on the windward corner decreases, in turn increasing the asymmetry in the distribution with rotation rate.

Pressure distributions at the last two axial stations along the forebody are shown in Fig. 18. Both stations show very good agreement between DES predictions and the measured values for both spin coefficients. As already indicated by the measurements,

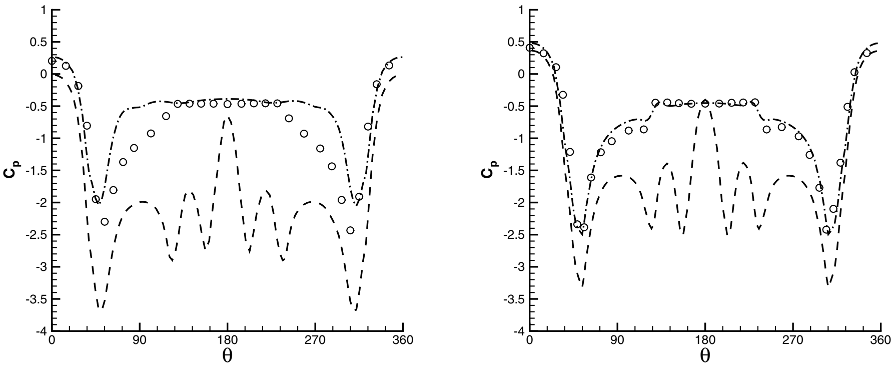

a) b)

Fig. 12 Pressure coefficient for $\alpha = 90$ deg at a) $x/L = 0.027$ and b) $x/L = 0.055$. ○: measurements; dash-dotted line: DES; dashed line: URANS.

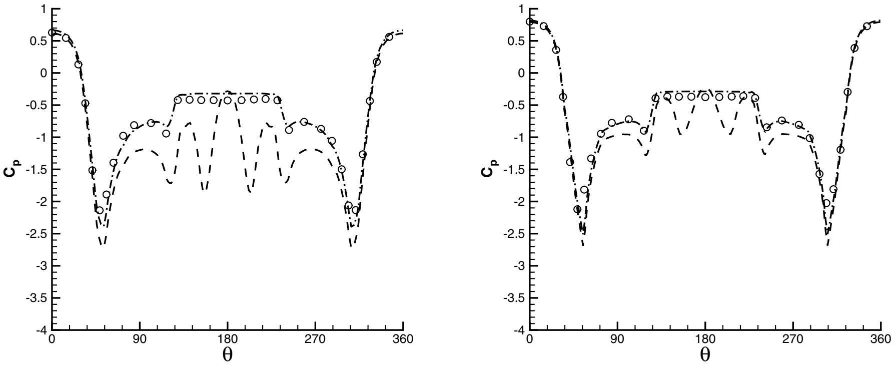

a) b)

Fig. 13 Pressure coefficient for $\alpha = 90$ deg at a) $x/L = 0.111$ and b) $x/L = 0.166$. ○: measurements; dash-dotted line: DES; dashed line: URANS.

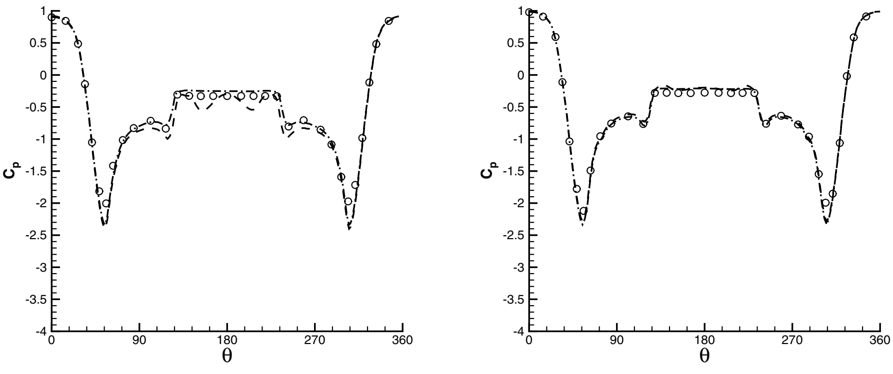

a) b)

Fig. 14 Pressure coefficient for $\alpha = 90$ deg at a) $x/L = 0.222$ and b) $x/L = 0.305$. ○: measurements; dash-dotted line: DES; dashed line: URANS.

DES predicts attached flow around the windward corners and in addition accurately captures the secondary minima induced by the interaction of the boundary layer with the leeward corners of the ogive. The uniform distribution along the leeward side in the separated region is also accurate. A comparison of the averaged side force and yawing moment in Table 3 for the static-geometry flow and the two rotating cases indicate increases in the magnitude of both quantities with increases in rotation rate, consistent with the behavior observed by Pauley et al. [9]. As also shown in the table, the axial and streamwise forces are essentially unaffected by rotation.

IV. Summary

DES and URANS were applied to the prediction of the massively separated flow around an ogive forebody characterized by a rounded cross section. Angles of attack of 60 and 90 deg were considered and for the highest Reynolds number at which measurements were acquired, $Re = 2.1 \times 10^6$. DES predictions of the pressure distribution for the static-geometry flow and ogive undergoing rotary motion (at $\alpha = 90$ deg) are for the most part in relatively good agreement with measurements, with improved agreement between simulation and experiment obtained for the static-geometry flow. The experimental database was used to supply the pressure distributions to which the simulations were compared. A more detailed assessment, for example, evaluating forces by integration of the measured pressures, should be useful especially because the ogive geometry was modeled in the simulations but not other aspects of the experiment such as the support sting. Because of limited resources, rotary-motion cases at $\alpha = 60$ deg were not undertaken but could be considered in future efforts since the experimental database includes such measurements.

For $\alpha = 60$ deg, the predicted flow structure in the wake using either URANS or DES is characterized by a pair of counter-rotating vortices that strongly influence the leeward pressure distribution.

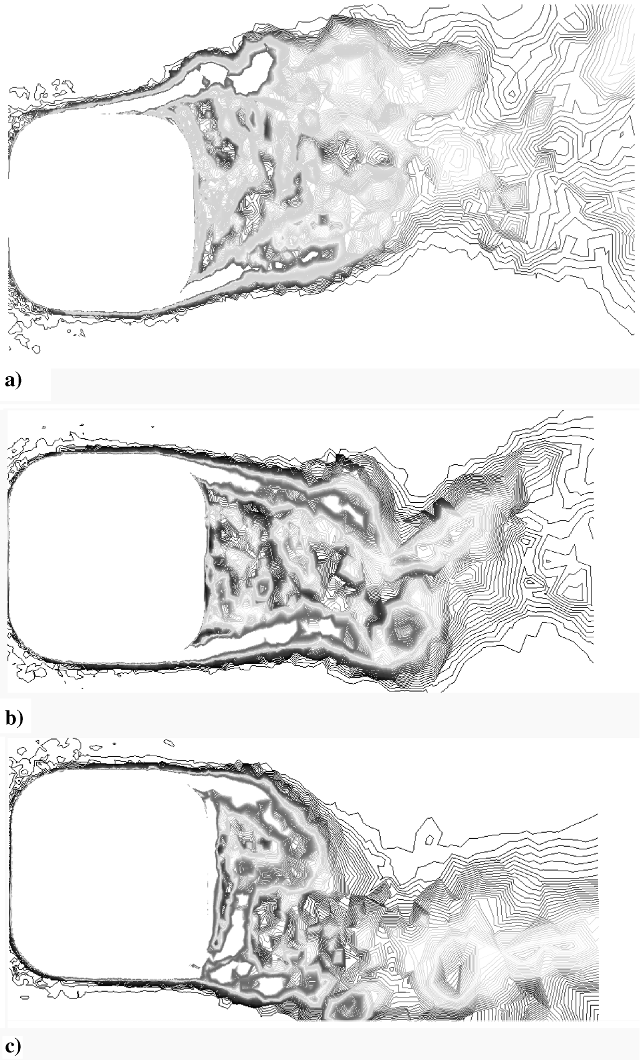

Fig. 15 Contours of the instantaneous vorticity magnitude in axial planes $x/L = 0.222$ a), $x/L = 0.5$ b), and $x/L = 0.805$ c). DES prediction of the flow with rotary motion, spin coefficient $\Omega D/(2U_\infty) = 0.2$.

The relatively coherent wake for $\alpha = 60$ deg resulted in URANS predictions of the pressure distribution on the forebody that were essentially the same as the DES results.

For the higher angle of attack, $\alpha = 90$ deg and the flow around the static geometry, DES predictions are in better agreement with measurements than the results obtained using unsteady RANS. URANS predictions indicate that the flow in the wake region is again characterized by a pair of counter-rotating vortices, analogous to the RANS predictions at $\alpha = 60$ deg. Strong three dimensionality in the aft region along the forebody is not recovered in the URANS, leading to a pressure distribution that has substantial variation, rather than the uniform distribution measured in the experiments reported by Pauley et al. [9] and accurately predicted in the DES.

The ogive undergoing rotary motion was computed using an ALE formulation, applied to the ogive for the present investigations for rotation about the model center at spin coefficients of 0.1 and 0.2. Visualizations of the vorticity magnitude in the leeward region showed the skewing of the wake by the rotation. Pressure distributions on the forebody exhibit adequate agreement with measured values, the asymmetry induced by the rotation being recovered and the overall variation with θ being captured in the DES, although the predictions were less satisfactory as compared to the static-geometry results. Factors that contribute to the discrepancies between the DES and experiments include regions of the laminar boundary layer that the simulations, by construction, will not account for. DES, being a hybrid RANS-LES method, remains subject to rather strong empiricism via boundary layer prediction that is under control of a RANS model in natural applications of the technique.

DES predictions of the static geometry were obtained for a range of mesh resolutions, the calculations showing that a wider range of scales is resolved with grid refinement. In general, the three dimensionality of the wake was stronger in the DES as compared to the RANS, consistent with related studies [6]. Though the wake structure did not exhibit as much axial (spanwise) variation in the URANS results, three dimensionality was present, an aspect that probably contributes to the relative agreement of the integrated and averaged streamwise force between the DES and URANS (see Shur et al. [17] for additional discussion). Strong differences in the time-dependent characteristics of the solutions were noted in the rms forces and moments. An additional and important difference between the DES and URANS noted in the current study was the pressure distribution along the forebody. This contributed not only to large differences in the axial force but would also influence quantities such as the pitching moment. These features are problematic for usage of URANS in flight applications focusing on areas such as control and stability, and such applications should benefit from the higher fidelity offered by DES.

Although the present contribution illustrates the usefulness of DES in a design application of the method, that is, as applied to massively separated flows, several topics remain worthy of additional and deeper investigations. Physical modeling challenges include the effects of laminar-to-turbulent transition. Numerical challenges include grid and time step effects. In the current work the influence of the mesh was extensively investigated; time steps for the computations were based on the criteria outlined in Spalart [18], with the time steps chosen such that the CFL number in the "focus region" comprising the separated wake was approximately unity. A time step study comparable to the grid refinement study reported in this work

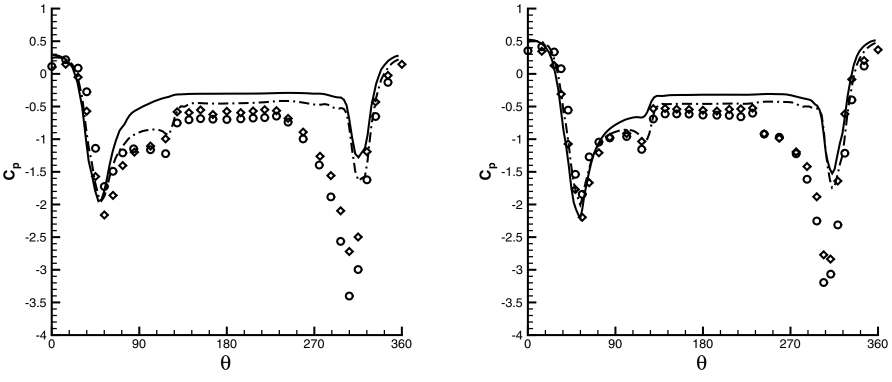

a) b)

Fig. 16 Pressure coefficient for $\alpha = 90$ deg at a) $x/L = 0.027$ and b) $x/L = 0.055$. $\Omega D/(2U_\infty) = 0.1$: ◇: measurements; solid line: DES. $\Omega D/(2U_\infty) = 0.2$: ○: measurements; dash-dotted line: DES.

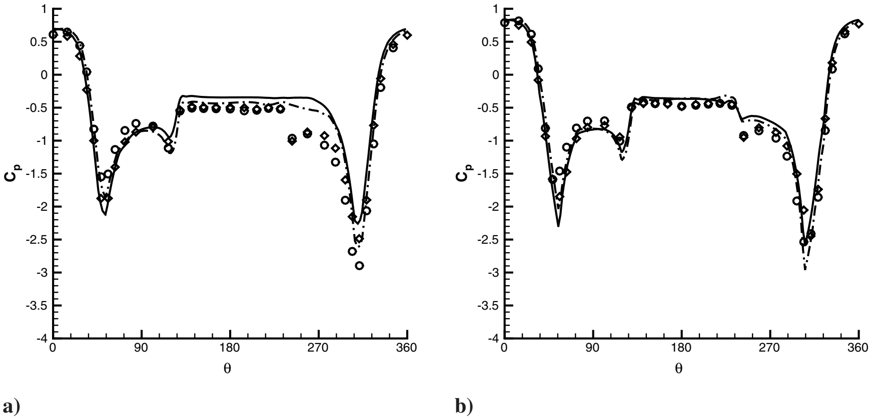

a) b)

Fig. 17 Pressure coefficient for $\alpha = 90$ deg at a) $x/L = 0.111$ and b) $x/L = 0.166$. $\Omega D/(2U_\infty) = 0.1$: ◇: measurements; solid line: DES. $\Omega D/(2U_\infty) = 0.2$: ○: measurements; dash-dotted line: DES.

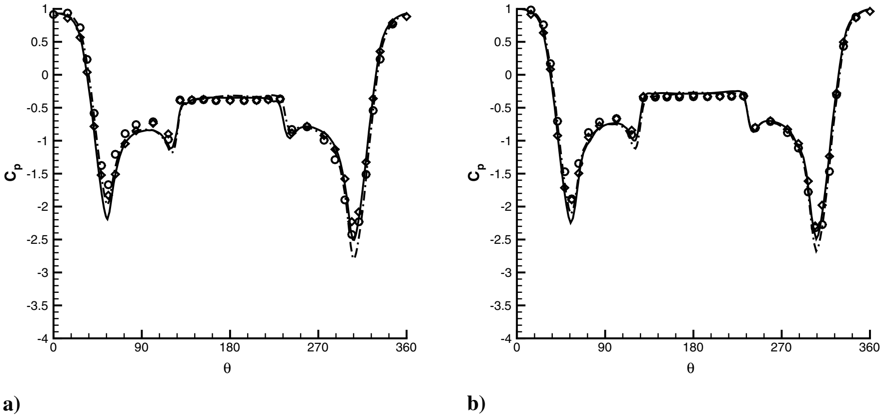

a) b)

Fig. 18 Pressure coefficient for $\alpha = 90$ deg at a) $x/L = 0.222$ and b) $x/L = 0.305$. $\Omega D/(2U_\infty) = 0.1$: ◇: measurements; solid line: DES. $\Omega D/(2U_\infty) = 0.2$: ○: measurements; dash-dotted line: DES.

Table 3 Predicted mean force and moment coefficients $\alpha = 90$ deg

Case	Axial force	Streamwise force	Side force	Yawing moment
Static geometry	0.0857	0.3212	0.0015	0.0017
$\Omega L/(2U_\infty) = 0.1$	0.0903	0.3393	0.0855	−0.0984
$\Omega L/(2U_\infty) = 0.2$	0.0882	0.3339	0.1931	−0.3171

would be useful to gauge sensitivity of DES predictions to the time step, a factor that might be especially important for the rotary-motion cases.

It is also worthwhile to emphasize that the superior accuracy of DES over URANS that has been typical of applications in massive separations is acquired at higher computational cost. In this work the same meshes and time steps were used in the URANS, rather than compute the URANS on coarser grids (in the wake, not the boundary layer) and using larger time steps which would be possible, in general. Optimizing the URANS for somewhat coarser grids and larger time steps lowers the computational cost of URANS over DES by roughly an order of magnitude.

The present computations were performed of the flow with fully turbulent boundary layers, accomplished by seeding the inflow condition with a small level of eddy viscosity that is sufficient to activate the turbulence model as the fluid entered the boundary layer. Measurements at lower Reynolds numbers exhibited sensitivity to the Reynolds number [9] and such regimes comprise an important and challenging test case for hybrid methods. Effects of transition to turbulence, possibly intermingled with boundary layer separation, are exceedingly difficult to model and accuracy requirements are typically very high.

Finally, aircraft forebodies are often asymmetric due to imperfections in the geometry, an effect that can produce a large yawing moment, even for configurations without sideslip. The strong yawing moment on low aspect ratio aircraft such as the F-15E can lead to relatively flat spins, for example. The computational methodologies under development and assessment in this work, while not fully complete, will be important for accurately modeling such phenomena.

Acknowledgments

The authors gratefully acknowledge the financial support of the Air Force Office of Scientific Research (Grant F49620-02-1-0117, Program Officers: Thomas Beutner and John Schmisseur). Bill Strang provided invaluable assistance with several aspects of the calculations including the coding of the ALE formulation. The experimental measurements were kindly provided by Mike Fremaux. The authors also gratefully acknowledge the helpful suggestions of Philippe Spalart. The calculations were performed at the DoD Maui High Performance Computing Center.

References

[1] Spalart, P. R., “Strategies for Turbulence Modelling and Simulation,” *International Journal of Heat Fluid Flow*, Vol. 21, No. 1, 2000, pp. 252–263.

[2] Spalart, P. R., Jou, W-H., Strelets, M., and Allmaras, S. R., “Comments on the Feasibility of LES for Wings, and on a Hybrid RANS/LES Approach,” *Advances in DNS/LES, 1st AFOSR International Conference on DNS/LES*, Greyden Press, Columbus, OH, 4–8 Aug. 1997.

[3] Spalart, P. R., and Allmaras, S. R., “A One-Equation Turbulence Model for Aerodynamic Flows,” *La Recherche Aerospatiale*, Vol. 1, No. 1, 1994, pp. 5–21.

[4] Batten, P., Goldberg, U., and Chakravarthy, S., "LNS—An Approach Towards Embedded LES," AIAA 2002-0427, 2002.

[5] Kawai, S., and Fuji, K., "Computational Study of a Supersonic Base Flow Using Hybrid Turbulence Methodology," *AIAA Journal*, Vol. 43, No. 6, 2005, pp. 1265–1275.

[6] Travin, A., Shur, M., Strelets, M., and Spalart, P. R., "Detached-Eddy Simulations Past a Circular Cylinder," *Flow, Turbulence, and Combustion*, Vol. 63, No. 1, 2000, pp. 293–313.

[7] Forsythe, J. R., Squires, K. D., Wurtzler, K. E., and Spalart, P. R., "Detached-Eddy Simulation of the F-15E at High Alpha," *Journal of Aircraft*, Vol. 41, No. 2, 2004, pp. 193–200.

[8] Constantinescu, G., and Squires, K. D., "Numerical Investigations of Flow over a Sphere in the Subcritical and Supercritical Regimes," *Physics of Fluids*, Vol. 16, No. 5, 2004, pp. 1449–1466.

[9] Pauley, H., Ralston, J., and Dickes, E., "Experimental Study of the Effects of Reynolds Number on High Angle of Attack Aerodynamic Characteristics of Forebodies During Rotary Motion," NASA CR 195033, 1995.

[10] van Dam, C. P., Saephan, S., Fremaux, C. M., and DalBello, T., "Prediction of Flows About Forebodies at High Angle of Attack Dynamics Conditions," *NATO/RTO Applied Vehicle Technology Panel Symposium on Advanced Flow Management: Vortex Flow and High Angle of Attack*, NATO, Brussels, 7–10 May 2001; also Paper No. MP-96-P39.

[11] Shur, M., Spalart, P. R., Strelets, M., and Travin, A., "Detached-Eddy Simulation of an Airfoil at High Angle of Attack," *4th International Symposium of Engineering Turbulence Modelling and Measurements*, Elsevier, Amsterdam, 24–26 May 1999.

[12] Strang, W. Z., Tomaro, R. F., and Grismer, M. J., "The Defining Methods of Cobalt$_{60}$: A Parallel, Implicit, Unstructured Euler/Navier-Stokes Flow Solver," AIAA 99-0786, 1999.

[13] Gottlieb, J. J., and Groth, C. P., "Assessment of Riemann Solvers for Unsteady One-Dimensional Inviscid Flows of Perfect Gases," *Journal of Computational Physics*, Vol. 78, No. 2, 1998, pp. 437–458.

[14] Karypis, G., Schloegel, K., and Kumar, V., "ParMETIS: Parallel Graph Partitioning and Sparse Matrix Ordering Library, Ver. 1.0," University of Minnesota, Department of Computer Science, Minneapolis, MN 55455, July 1997.

[15] Geuzaine, P., Grandmont, C., and Farhat, C., "Design and Analysis of ALE Schemes with Provable Second-Order Time-Accuracy for Inviscid and Viscous Flow Simulations," *Journal of Computational Physics*, Vol. 191, No. 1, 2003, pp. 206–227.

[16] Pirzadeh, S., "Three-Dimensional Unstructured Viscous Grids by the Advancing Layers Method," *AIAA Journal*, Vol. 34, No. 1, 1996, pp. 43–49.

[17] Shur, M., Spalart, P. R., Squires, K. D., Strelets, M., and Travin, A., "Three-Dimensionality in Reynolds-Averaged Navier-Stokes Solutions Around Two-Dimensional Geometries," *AIAA Journal*, Vol. 43, No. 6, 2005, pp. 1230–1242.

[18] Spalart, P. R., "Young Person's Guide to Detached-Eddy Simulation Grids," NASA CR-2001-211032, 2001.

K. Fujii
Associate Editor